Impact of thixotropy on flow patterns induced in a stirred tank: Numerical and experimental studies

G. Couerbe[a], D.F. Fletcher[b], C. Xuereb[a], M. Poux[a,*]

[a] Université de Toulouse, Laboratoire de Génie Chimique, CNRS/INP/UPS, 5 rue Paulin Talabot, BP 1301, 31106 Toulouse Cedex, France
[b] School of Chemical and Biomolecular Engineering, The University of Sydney, NSW 2006, Australia

Keywords:
Thixotropy
CFD
PIV
Stirred tank
Impeller
Mixing

A B S T R A C T

Agitation of a thixotropic shear-thinning fluid exhibiting a yield stress is investigated both experimentally and via simulations. Steady-state experiments are conducted at three impeller rotation rates (1, 2 and 8 s^{-1}) for a tank stirred with an axial-impeller and flow-field measurements are made using particle image velocimetry (PIV) measurements. Three-dimensional numerical simulations are also performed using the commercial CFD code ANSYS CFX10.0. The viscosity of the suspension is determined experimentally and is modelled using two shear-dependant laws, one of which takes into account the flow instabilities of such fluids at low shear rates. At the highest impeller speed, the flow exhibits the familiar outward pumping action associated with axial-flow impellers. However, as the impeller speed decreases, a cavern is formed around the impeller, the flow generated in the vicinity of the agitator reorganizes and its pumping capacity vanishes. An unusual flow pattern, where the radial velocity dominates, is observed experimentally at the lowest stirring speed. It is found to result from wall slip effects. Using blades with rough surfaces prevents this peculiar behaviour and mainly resolves the discrepancies between the experimental and computational results.

1. Introduction

Mixing of thixotropic fluids is common in the food, polymer and pharmaceutical industries. Thixotropy is generally defined as a progressive decrease in viscosity over time for a constant applied shear stress, followed by gradual recovery when this stress is removed. Thixotropic deformable materials thus exhibit a complex non-Newtonian rheological behaviour comprising shear-thinning, a time-dependant viscosity and a yield stress. Although the concept of yield stress is often challenged, its physical approximation has proved very useful as a key design tool in a wide range of engineering applications, including mixing. However, the basic hydrodynamic phenomena occurring in three-dimensional flows in stirred tanks with such materials are at best partially understood. As a consequence determination of the effectiveness, design, optimization and scale-up of these processes are extremely uncertain. For example, agitation of fluids exhibiting a yield stress results in the formation of a region of relatively rapid motion around the impeller (called a cavern where high shear rates prevail) and essentially stagnant regions elsewhere in the vessel. Moreover, the yield stress cannot be considered separately from thixotropy because these two phenomena are the result of the jamming and unjamming of the microstructure of a number of typical yield stress fluids (gels, clay suspensions, colloidal glasses). The mechanical behaviour of these systems consequently results from the competition between aging (spontaneous restructuration at rest) and shear 'rejuvenation' (destruction of the microstructure under shear). As stated by Coussot et al. (2002), the viscosity then jumps in a discontinuous manner to infinity at a critical stress, contrary to the continuous progression anticipated for 'ideal' yield stress fluids. Consequently, when a constant shear rate below the critical one is applied to the material the flow is unstable: the material will either fracture or produce shear-banding instabilities (Pignon et al., 1996). However, these basic phenomena are seldom taken into account and the existing empirical models need experimental validation. The aims of this work are twofold.

* *Corresponding author.*
E-mail address: martine.poux@ensiacet.fr (M. Poux).

Nomenclature

a	restructuration at rest (s^{-1})
b	shear rejuvenation (s^{m-1})
C	impeller off-bottom clearance (m)
$\mathbf{D}$	strain tensor (s^{-1})
D_{II}	second invariant of the strain tensor (s^{-1})
D	impeller diameter (m)
dt	exposure time delay (s)
Fl	Flow number (dimensionless)
K	fluid consistency coefficient (Pa s^n)
m	power-law index in the structural-state function (dimensionless)
M	Papanastasiou's parameter (s)
M′	modified Papanastasiou's parameter (s^n)
n	power-law index in Coussot's model (dimensionless)
n_1	power-law index in H–B model (dimensionless)
N	impeller speed (s^{-1})
p	pressure (Pa)
Q_a	axial volumetric flow rate ($m^3\,s^{-1}$)
Q_r	radial volumetric flow rate ($m^3\,s^{-1}$)
r	distance from tank centre (m)
R	tank radius (m)
Re	Reynolds number (dimensionless)
T	tank diameter (m)
tr	signifies the trace of the tensor
$\mathbf{v}$	velocity vector ($m\,s^{-1}$)
v_r	radial velocity ($m\,s^{-1}$)
v_{tip}	blade tip velocity ($m\,s^{-1}$)
v_z	axial velocity ($m\,s^{-1}$)
V	volume swept by the impeller (m^3)
V_c	cavern volume (m^3)
x	mechanism of thixotropic recovery (dimensionless)
z	height from tank bottom (m)

Greek letters

$\dot{\gamma}$	shear rate (s^{-1})
$\dot{\gamma}'$	modified shear rate (s^{-1})
$\boldsymbol{\delta}$	unity tensor (dimensionless)
ε	penalty factor (s^{-1})
η	apparent viscosity (Pa s)
η_∞	apparent viscosity at infinite shear rate (Pa s)
λ	structural-state parameter (dimensionless)
ρ	density ($kg\,m^{-3}$)
$\boldsymbol{\tau}$	viscous stress tensor (Pa)
τ_{II}	second invariant of the viscous stress tensor (Pa)
τ	shear stress (Pa)
τ_Y	apparent yield stress (Pa)

Subscripts

min	minimum
eq	equilibrium

Superscripts

T	transpose

- Firstly, PIV techniques are used to characterize the steady-state flow fields obtained in a stirred tank with a thixotropic fluid (an aqueous suspension of laponite, a colloidal glass). The mixing efficiency of the impeller is also quantified in terms of its pumping capacity, the created cavern volume and the ratio of the axial to radial flow-rates;
- Secondly, the ability of CFD to predict 3D flows of such fluids in stirred tanks is investigated and an assessment is made of the need to account for flow instabilities at low shear rates in such simulations. The rheological behaviour of the model fluid has first to be determined, then modelled (taking account or not of the basic flow instability) and then it must be implemented in the CFD code.

2. Methods and materials

2.1. *Experimental setup*

The material chosen for investigation was a 3 wt.% suspension (in distilled water) of laponite. This synthetic hectorite clay (Laponite RD, Laporte Industries) produces clear colloidal anionic dispersions exhibiting shear-thinning, thixotropy and a yield stress (Poole and Escudier, 2003). The chemical structure of this clay is detailed in the work of Escudier and Presti (1996). As colloidal interactions between solid particles drive the mechanical behaviour of clay-water mixtures, controlling both the pH and the ionic strength of these suspensions is essential. Thus, the desired quantity of Laponite was added under vigorous stirring ($N = 9\,s^{-1}$) to distilled water then, one hour later (the time necessary for the powder to be dispersed), 6 ppm of salt (NaCl) was introduced and stirring was maintained for a further hour. At this stage, the pH of the suspension was close to 10 and its value was reproducible. Dissolution of Laponite was thus negligible because the pH was higher than 8.5 (Thompson and Butterworth, 1992). Then the preparation was left at rest for four days to ensure complete absorption of the water molecules into the solid matrix. This precaution prevents (Ferroir et al., 2004) irreversible aging from occurring which has the potential to change the measurements significantly during the experiments.

Then this suspension was characterized using a stress-controlled cone-plate rheometer (Carrimed CSL2 500, TA Instruments). The cone-plate was 60 mm in diameter and the cone angle was 2°. A temperature of $25 \pm 0.1\,^{\circ}C$ was set during the rheological measurements and a solvent trap was always used to minimize sample evaporation. To avoid wall slip effects, tools with rough surfaces were used. The impact of these complicating effects on rheological experiments with such complex fluids is detailed in Coussot et al. (1993). Measurements of viscometric properties were obtained using a procedure which could reliably produce a consistent shear history of the fluid. In order to reduce the impact of the pre-test flow history on the measurements, samples were first pre-sheared for 600 s at a shear rate of $1000\,s^{-1}$ and then left at rest during 60 s before any measurements were made. The chosen de-structurization methodology was based on that of Willenbacher (1996), who also used a high shear rate to pre-treat the fluid and tests performed by us showed that a viscosity plateau was not attained before 300 s of pre-shear, even at a shear strain of $1000\,s^{-1}$. Complete rest was not chosen as the initial state of reference because laponite suspensions have a very long characteristic time of evolution from rest (Bonn et al., 2002). Rather a flow-equilibrium procedure was adopted, whereby a shear rate was imposed during an appropriate time interval before being raised. The shear rate was increased logarithmically from 0.5 to $2390\,s^{-1}$ with

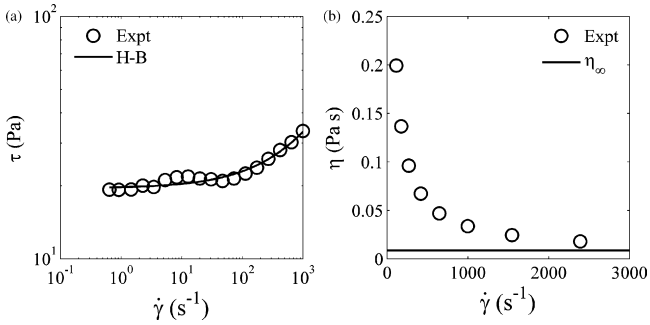

Fig. 1 – Rheological characterization of the suspension. (a) Equilibrium flow curve (EFC): comparison between experimental results and the fitted H–B model. (b) The apparent viscosity tends towards 0.0087 Pa s as the shear rate tends to infinity.

20 measurement points. A steady-state was assumed to be reached when increasing the measurement time resulted in no significant change in the measured viscosities. Therefore, a maximum time interval of 60 s was chosen.

Fig. 1 shows the results in terms of a shear-dependant stress (Fig. 1a) and shear-dependant viscosity (Fig. 1b). The resulting fitted curve (Fig. 1a) corresponds to the well-known Herschel–Bulkley (H–B) model:

$$\tau = \tau_Y + K\dot{\gamma}^{n_1} \tag{1}$$

where $\tau_Y = 19.6\,\text{Pa}$ is the yield stress, $K = 0.21\,\text{Pa}\,\text{s}^{n_1}$ is the consistency parameter and $n_1 = 0.61$ is the power-law index. Moreover, this flow curve also displays a minimum stress (and consequently a decreasing part) with coordinates:

$$(\dot{\gamma}_{\min}, \tau_{\min}) = (47.1\,\text{s}^{-1},\ 21\,\text{Pa}) \tag{2}$$

These phenomena are impossible to reproduce using an "ideal" yield stress model for the fluid, as has already been highlighted by Pignon et al. (1996). A simple linear stability analysis (McDonald and Anderson, 1996) shows that if the flow curve exhibits a decreasing part, the corresponding flows are unstable. Consequently, stable homogeneous flows can occur only when the constant shear stress applied to the material is higher than a critical value. This behaviour is characteristic of a certain category of thixotropic fluids (Cheng, 2003) and can be modelled by the means of two equations: the first, Eq. (3), describes the kinetics of evolution of a single scalar structural-state parameter of the material, λ, and the second, a general viscosity function, relates the flow and structure.

$$\frac{d\lambda}{dt} = a(1 - x\lambda) - b\lambda\dot{\gamma}^m \tag{3}$$

where x is a parameter which relates to the mechanism of thixotropic recovery: setting $x = 0$ means that the recovery rate is independent of the current structure and shear rate. Eq. (3) actually describes the competition between aging (spontaneous rebuilding of the microstructure at rest) and progressive rejuvenation (destruction of this microstructure) by the shear flow. The homogeneous flow of such a material in steady-state is related by Eqs. (4) and (5):

$$\frac{d\lambda}{dt} = 0 \tag{4}$$

$$\lambda_{eq} = \frac{1}{x + (b/a)\dot{\gamma}^m} \tag{5}$$

The model of Coussot et al. (2002) was primarily chosen because it has been tested successfully for a wide range of materials (glassy systems and colloidal glasses), including laponite suspensions:

$$x = 0;\ m = 1;\ \eta = \eta_\infty(1 + \lambda^n) \tag{6}$$

Then according to Eqs. (5) and (6), the shear stress of the equilibrium flow curve (EFC) and the coordinates of its minimum are:

$$\tau = \eta_\infty\left(\frac{a}{b}\right)^n \dot{\gamma}^{1-n} + \eta_\infty\dot{\gamma} = \left(\frac{\eta_\infty(a/b)^n}{\dot{\gamma}^n} + \eta_\infty\right)\dot{\gamma} \tag{7}$$

$$(\dot{\gamma}_{\min}, \tau_{\min}) = \left(\frac{a}{b}(n-1)^{1/n},\ \frac{a}{b}\eta_\infty n(n-1)^{(1/n)-1}\right) \tag{8}$$

Thus, measuring the viscosity at infinite shearing, η_∞, (Fig. 1b) and knowing the characteristics of the minimum in the EFC (Eq. (2)) allows determination of the model parameters a/b and n. In our case:

$$\eta_\infty = 0.0087\,\text{Pa}\,\text{s};\quad n = 1.02;\quad \frac{a}{b} = 2200\,\text{s}^{-1} \tag{9}$$

PIV measurements were performed in a conical-bottomed cylindrical tank with the geometry defined in a standard way. Its diameter, T, was equal to 0.19 m. A Mixel TT agitator (Mixel, Dardilly, France), with a diameter equal to $D = 0.5\,T$, was mounted on a vertical shaft. The impeller clearance was $C = 0.33\,T$, where C is defined as the distance from the vessel bottom to the lowest horizontal plane swept by the impeller. The cylindrical tank was placed inside a square tank, whose front panel was made of Altuglass™ to allow distortion-free measurements. This square tank was filled with water in order to minimize refraction at the cylindrical surface of the inner vessel. The PIV measurements were taken on a vertical plane midway between two baffles. For practical reasons, only the dimensionless heights z/R ranging from 0.35 to 1.4 were investigated ($0 \le z/R \le 2$).

The velocity measurements were taken using a LaVision system (LaVision GmbH, Goettingen, Germany), the design of which is detailed in the work of Aubin et al. (2004). Images were acquired at 4.95 Hz with an exposure time delay which depended on the selected rotation velocity of the impeller ($dt_{1\,s^{-1}} = 1.2 \times 10^{-2}$ s; $dt_{2\,s^{-1}} = 5.5 \times 10^{-3}$ s; $dt_{8\,s^{-1}} = 7 \times 10^{-4}$ s). The spatial resolution of the PIV measurements was 2 mm × 2 mm. The instantaneous velocity data obtained from 50 image pairs were used to determine the time-averaged radial-axial velocity fields. The yield surfaces were assumed to coincide with the locus of points where the local measured velocity was equal to 10^{-3} m s^{-1}. A similar criterion has already been used by Amanullah et al. (1998).

2.2. *Computational methods*

The numerical simulation of the flow in the stirred vessel was performed using ANSYS-CFX 10.0. This is a general-purpose commercial CFD package that solves the Navier–Stokes equations using a finite volume method via a coupled solver. The

conservation equations solved are given below:

$$\nabla \cdot (\rho \mathbf{v}) = 0 \tag{10}$$

$$\nabla \cdot (\rho \mathbf{v} \otimes \mathbf{v}) = -\nabla p + \nabla \cdot \boldsymbol{\tau} \tag{11}$$

$$\boldsymbol{\tau} = \eta \left(\nabla \mathbf{v} + (\nabla \mathbf{v})^{\mathrm{T}} - \frac{2}{3} \boldsymbol{\delta} \nabla \cdot \mathbf{v} \right) \tag{12}$$

where $\mathbf{v}$ is the velocity vector, ρ the density of the fluid, p the pressure and $\boldsymbol{\tau}$ is the viscous stress tensor. The superscript T denotes the transpose operation. Incompressible, generalized Newtonian fluids with shear-dependant viscosity were considered:

$$\boldsymbol{\tau} = 2\eta(D_{\mathrm{II}})\mathbf{D} \tag{13}$$

where $\mathbf{D}$ is the strain tensor defined as $\mathbf{D} = \frac{1}{2}[\nabla \mathbf{v} + (\nabla \mathbf{v})^{\mathrm{T}}]$. D_{II} is the second invariant of $\mathbf{D}$ and it is defined as $D_{\mathrm{II}} = -1/2 \mathrm{tr}\, \mathbf{D}^2$, where tr stands for the trace. The shear rate $\dot{\gamma}$ is defined as $\dot{\gamma} = 2\sqrt{-D_{\mathrm{II}}}$.

Both the H–B and Coussot models require a numerical approximation to regularize the infinite viscosity in shear-free regions (where the viscous stress tensor is ill-defined). For instance, the tensorial form of the H–B model can be expressed as:

$$\boldsymbol{\tau} = 2 \left(\frac{\tau_{\mathrm{Y}}}{\dot{\gamma}} + K \dot{\gamma}^{n_1 - 1} \right) \mathbf{D} \text{ for } |\tau_{\mathrm{II}}| > \tau_{\mathrm{Y}}^2 \tag{14}$$

$$\mathbf{D} = 0 \text{ for } |\tau_{\mathrm{II}}| \leq \tau_{\mathrm{Y}}^2 \tag{15}$$

where τ_{II} is the second invariant of the viscous stress tensor.

The constitutive Eqs. (14) and (15) apply on each side of a yield surface. They are very difficult to implement for computational analysis in complex geometries, due to the necessity to track surfaces between yielded and unyielded regions at an *a priori* unknown location (Beris et al., 1985). Hence to deal with this singular behaviour, some authors have modified Eq. (14) so as to make it valid in both yielded and unyielded regions. These regularized laws were primarily designed to account for Bingham plastic behaviour (where $n_1 = 1$, $K = \eta_\infty$). The biviscosity model (O'Donovan and Tanner (1984)) treats the unyielded state as a Newtonian fluid of very high viscosity. In this way, the viscous stress tensor is unambiguously defined at vanishing shear rates but tracking of the yield surface is not avoided because two different viscosities are involved (Papanastasiou and Boudouvis, 1997). Eliminations of this tracking can be obtained either by adding a penalty-like factor, ε, to the shear rate that is applied everywhere ($\dot{\gamma}' = \dot{\gamma} + \varepsilon$, Bercovier and Engelman, 1980) or by introducing a correction factor (Papanastasiou, 1987):

$$\boldsymbol{\tau} = 2 \left(\frac{\tau_{\mathrm{Y}} \left(1 - \exp(-M\dot{\gamma})\right)}{\dot{\gamma}} + \eta_\infty \right) \mathbf{D} \tag{16}$$

The exponent M has dimensions of time and controls the stress growth such that below the apparent yield stress τ_{Y} a finite stress is calculated for vanishingly small shear rates. In the limiting case of $M \to +\infty$, this model reduces to the Bingham model in the yielded region. The accuracy and effectiveness of the Papanastasiou model have been demonstrated by many researchers (for a brief review, see Alexandrou et al., 2003). In addition, at vanishing shear rates, the apparent viscosity in the Bingham model becomes infinite, which leads to a discontinuity and numerical difficulties. These problems are avoided by using any of the three regularization models because the viscosity is then automatically bounded. This makes the regularization ambiguous for H–B fluids, therefore Eq. (16) is often generalized by specifying $\eta_\infty = K\dot{\gamma}^{n_1 - 1}$ (Arratia et al., 2006). Then the viscosity is unbounded but it is desirable to have a generalized model that overcomes this problem (Zhu et al., 2005). It was overcome here using the following expression for a H–B fluid:

$$\boldsymbol{\tau} = 2 \left(\frac{\tau_{\mathrm{Y}} (1 - \mathrm{e}^{-M\dot{\gamma}})}{\dot{\gamma}} + K \max\left(\dot{\gamma}, 10^{-6}[\mathrm{s}^{-1}]\right)^{n_1 - 1} \right) \mathbf{D} \tag{17}$$

Following Papanastasiou's idea, the Coussot model expresses:

$$\boldsymbol{\tau} = 2 \left(\frac{n_\infty (a/b)^n (1 - \exp(-M'\dot{\gamma}^n))}{\dot{\gamma}^n} + \eta_\infty \right) \mathbf{D} \tag{18}$$

A preliminary study showed that for $M \geq 500$ s ($M' \geq 500\,\mathrm{s}^n$) results were independent of the value of M (M') and therefore M (M') was set to 500 s ($500\,\mathrm{s}^n$).

When there was no interaction between the blades and baffles, the computations were conducted in a rotating frame containing the impeller. This geometry was represented by an unbaffled 120° section containing just one impeller blade; periodicity was assumed in the azimuthal direction. Vector fields were averaged on sixteen equidistant vertical planes. When there were interactions between the blades and the baffles, the impeller motion was accounted for using a Multiple Reference Frame technique. Hence the tank was divided into two zones, one around the impeller being a rotating frame of reference (where the impeller appears stationary) and the other one being stationary. These zones were connected using a "frozen rotor" model that performs the frame change model by mapping results from one frame to the other for a fixed relative position of the rotating and stationary domains. Four simulations, corresponding to four relative positions between the blades and the baffles, were carried out (0°, 7.5°, 15°, 22.5°). Vector fields were averaged on the sixteen vertical planes midway between two consecutive baffles.

A preliminary grid convergence study was carried out in order to verify that the solution was grid independent. Meshes composed of approximately 80,000 and 300,000 nodes were used to model one third and the entire vessel, respectively. No-slip boundary conditions were applied at the vessel walls and the impeller. The liquid free surface was modelled with zero-flux and zero-stress conditions. The advection terms in each equation were discretized using a bounded second-order differencing scheme. The simulations were typically considered converged when the root mean square residuals for all quantities fell below 10^{-6} and when fluid velocities and viscosities calculated at nine different loci throughout the vessel remained unchanged with further iterations. As non-Newtonian models were unavailable in the CFD code, shear-dependant viscosities were introduced using user-defined functions.

3. Results and analyses

The system performance and flow characterization are based on both qualitative and quantitative parameters, namely:

Table 1 – Quantification of the impeller performance

	$N = 1\,s^{-1}$			$N = 2\,s^{-1}$			$N = 8\,s^{-1}$		
	Experiment	H–B	Coussot	Experiment	H–B	Coussot	Experiment	H–B	Coussot
Fl	0.02	0.02	0.02	0.13	0.03	0.03	0.62	0.46	0.48
Q_a/Q_r	0.78	0.38	0.35	1.4	0.73	0.68	3.1	2.8	3.2
V_c/V	3.4	1.9	1.5	9.8	2.6	1.9	–	17.0	18.4

The experimental data are compared with those obtained using the two different models for the fluid rheology in the CFD simulations.

- Flow patterns: measured velocities below the cavern-defining velocity were not accounted for and the remaining velocity data were normalized by the theoretical blade tip speed v_{tip} ($v_{tip} = \pi ND$).
- The flow number, Fl, the normalized volume of the caverns, V_c/V, (V being the volume swept by the impeller) and the ratio of the axial to the radial flow, (Q_a/Q_r), passing through the volume swept by the impeller were determined. These parameters, summarized in Table 1, were calculated from the ensemble-averaged data to allow comparison between the simulation and experimental results.

4. Experimental results

In order to ensure the experimental results were repeatable and were produced under controlled conditions, the flow number was calculated for twenty measurements at the same conditions ($N = 1\,s^{-1}$) and the pumping number was found to be 0.017 ± 0.005, showing that the results are indeed repeatable. The flow fields were also observed to be very similar.

Fig. 2 shows the two-dimensional velocity fields determined for $N = 1\,s^{-1}$, $N = 2\,s^{-1}$ and $N = 8\,s^{-1}$. These conditions were chosen primarily because very different flows occurred. Indeed, at the highest rotation velocity ($N = 8\,s^{-1}$; Fig. 2c), the flow pattern and the flow number, Fl, are similar to those observed for the Mixel TT running in the turbulent regime with a Newtonian fluid (Aubin et al., 2001; Fl = 0.67). A primary circulation loop exists in the lower part of the tank and extends half way up the vessel (compared with almost three-quarters of the way up in the case of a turbulent regime with a Newtonian fluid). In the upper half of the tank, the liquid velocities are low and circulation is poor. Just below the centre of the impeller a region of up-flowing liquid exists, which is evidence of a secondary recirculation loop. Due to the conical bottom of the vessel, this entire secondary circulation loop could not be captured using the PIV. The flow is induced from above the impeller and mainly leaves it in the vertical downward direction. As a consequence, more than 75% of the volumetric flow rate passes through the impeller swept volume in an axial manner (Table 1: $Q_a/Q_r = 3.1$).

When the rotation rate is lowered to $2\,s^{-1}$ (Fig. 2b), the velocity vectors show the appearance of an ellipsoidal-shaped cavern surrounding the volume swept by the impeller. Both circulation loops are still present but the difference between the magnitudes of their velocities has become insignificant. This also results in the displacement of the circulation centres towards the impeller swept volume and hence in modifying the flow pattern in the vicinity of the impeller. The flow is induced from above the impeller again but it is now discharged weakly at about 45° from the vertical in the downward direction and strongly in the radial direction. This flow reversal in the radial direction makes the lateral surface of the impeller swept volume of primary importance and results in a 55% reduction in Q_a/Q_r (Table 1, $Q_a/Q_r = 1.4$). This reorganization takes place together with the reduction of the magnitude of the velocity (note the change in the velocity scale vector at the top of Fig. 2b) and with a breakdown in the pumping capacity (Fl = 0.13). This breakdown has also been observed in tanks agitated by a Rushton turbine by Ranade (1997), Lamberto et al. (1999) and Rice et al. (2006) with Newtonian fluids in experiments and in simulations. Rice et al. (2006) observed a radially reciprocating motion at $Re = 1$, with negligible net pumping but they did not observe any overall flow reversal. Their analysis of the forces acting on a fluid element in the radial direction indicated that the derivative of the radial velocity near the blade tip was negligible (contrary to what happens in the turbulent regime). Moreover, Nouri and Whitelaw (1990) found

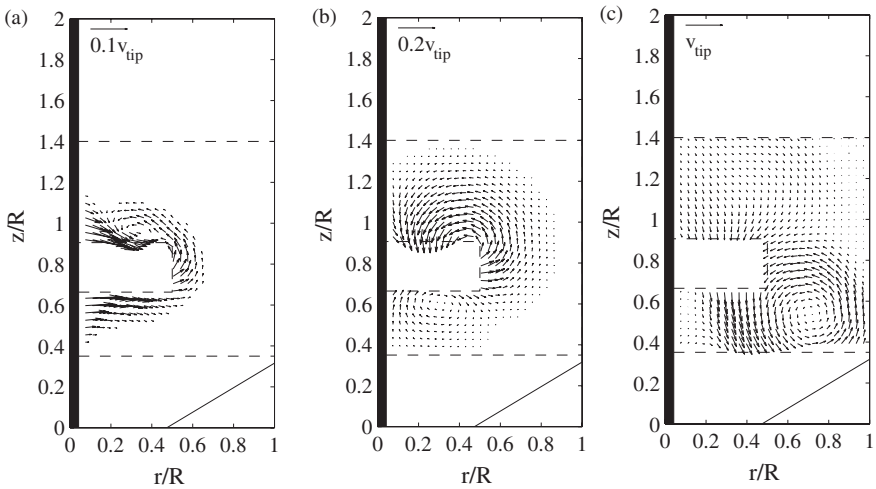

Fig. 2 – Experimental flow patterns on an axial-radial plane for different impeller rotation rates. (a) $N = 1\,s^{-1}$. (b) $N = 2\,s^{-1}$. (c) $N = 8\,s^{-1}$.

from laser-Doppler anemometry measurements that the discharge angle of the flow leaving a pitched-blade impeller in the downward direction varied with Reynolds number or with the modified Reynolds number (which is a generalization of the Reynolds number suitable for shear-thinning fluids) in the same way. The changes observed in the vicinity of the impeller were believed to be due mainly to the flow regime rather than to the particular nature of the fluids.

When the impeller rotation rate is lowered to $1\,s^{-1}$ (Fig. 2a), the cavern dimensions are greatly reduced and the movement is localized near the impeller. The pumping capacity vanishes (Fl = 0.02) and the volumetric flow rate passing through the impeller swept volume is now primarily in the radial direction (Table 1, $Q_a/Q_r = 0.78$). The flow field near the impeller tip remains almost identical. Surprisingly, the main changes occur near the lower and upper planes swept by the impeller, where the vertical velocity component is negligible. To the best of the authors' knowledge, the latter behaviour has not been reported previously in the literature.

4.1. *CFD predictions versus experimental data*

The computational ensemble-averaged velocity fields are shown in Fig. 3. Both models give similar results. The parameters identified in Table 1 also indicate that the agreement is generally good, especially for the flow numbers and the Q_a/Q_r ratios. This tendency suggests that predictions are model-independent in the vicinity of the impeller, where the shear is the highest. The computational results are consistent with the experimental data, as the breakdown of the pumping capacity and the transition from axial to radial flow around the impeller swept volume are predicted well. Moreover, taking account or not of flow instabilities at small shear rates in the simulations only changed the predictions far from the impeller. Then the localization of the sheared/unsheared zone, as well as the cavern volume, is model-dependant. The observed discrepancies, especially for the rotation rate of $2\,s^{-1}$, are believed to arise because of the very rapid change of behaviour with rotation rate over the considered range. As the impeller speed is increased from the minimum to the maximum value there is a very abrupt change from a small cavern surrounding the blade to almost the entire fluid mass in the vessel being in motion. In such a situation, small experimental or modelling errors give rise to very different behaviour in the region of rapid change. At the highest rotation velocity ($N = 8\,s^{-1}$), the calculated velocity field shows the key features of the flow, such as the location of the recirculation regions (both principal and second circulation loops) and the magnitude of the velocity. There is also relatively good agreement between the predicted and experimental quantitative data (Table 1).

Fig. 4 shows a comparison between experiments and predictions of the normalized axial velocity v_z/v_{tip} at the lowest plane swept by the impeller, as a function of the normalized radial distance from the tank centre. The ability of both models to quantitatively predict flow in the vicinity of the impeller is confirmed. However, significant discrepancies appear as the rotation rate is reduced (Table 1, Figs. 2 and 3). In fact, the two lowest rotation rates examined pose the greatest difficulty both from the experimental and the computational points of view. Fig. 5 shows a comparison of the normalized axial velocity v_z/v_{tip} measured at the lowest plane swept by

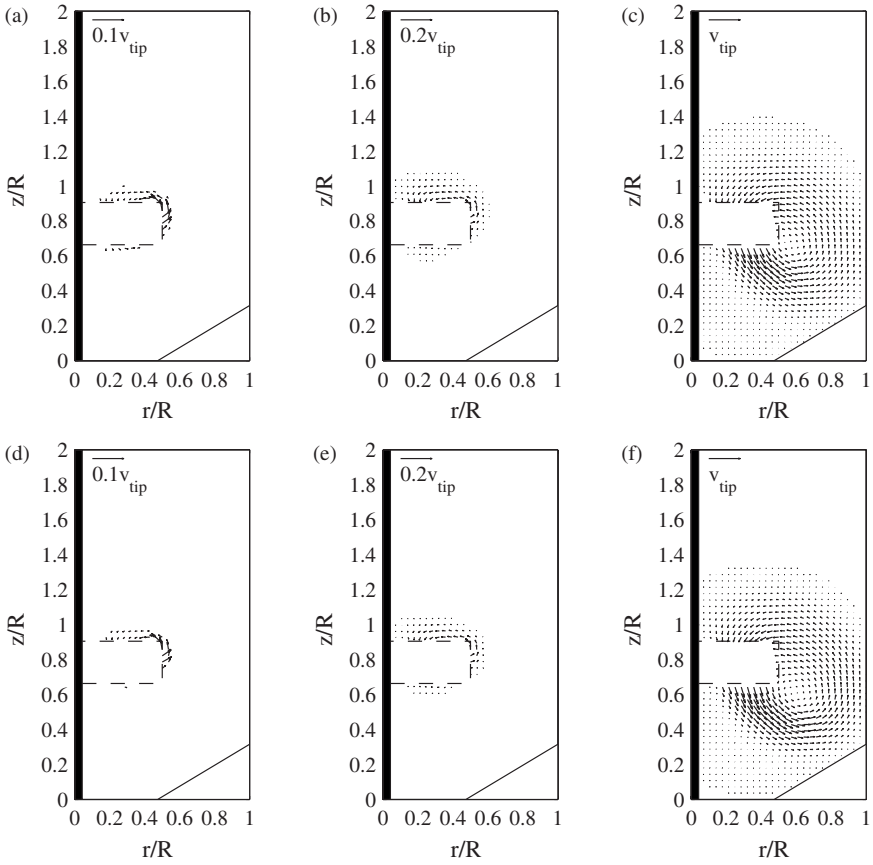

Fig. 3 – Influence of the rheological model on the computed flow patterns in the axial-radial plane. (a) H–B, $N = 1\,s^{-1}$. (b) H–B, $N = 2\,s^{-1}$. (c) H–B, $N = 8\,s^{-1}$. (d) Coussot, $N = 1\,s^{-1}$. (e) Coussot, $N = 2\,s^{-1}$. (f) Coussot, $N = 8\,s^{-1}$.

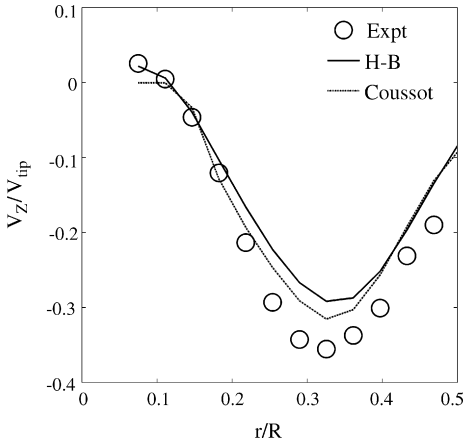

Fig. 4 – Comparison between the experimental data and the predictions of the normalized axial velocity v_z/v_{tip} at the lowest plane swept by the impeller (z/R = 0.64) as a function of the normalized radial distance r/R from tank centre.

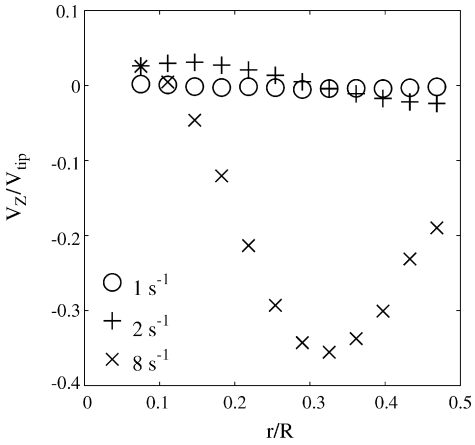

Fig. 5 – Comparison of the normalized axial velocity v_z/v_{tip} measured at the lowest plane swept by the impeller (z/R = 0.64) as a function of the normalized radial distance from tank centre r/R for $N = 1\ s^{-1}$ (×), $N = 2\ s^{-1}$ (o) and $N = 8\ s^{-1}$ (+).

the impeller as a function of the normalized radial distance from the tank centre for $N = 1\ s^{-1}$, $N = 2\ s^{-1}$ and $N = 8\ s^{-1}$. The maximum axial velocity measured at the lowest plane of the impeller swept volume is around 0.5 and 3% of the tip velocity for $N = 1\ s^{-1}$ and $N = 2\ s^{-1}$ (1.5×10^{-3} and $10^{-2}\ m\ s^{-1}$, respectively). These velocities are very low and hence the average displacement of the particles in the interrogation windows is tiny even if the delay between pulses of the light sheet is rather long. The combination of these two limitations results in a significant uncertainty in the absolute velocities measured. Computationally speaking, small convective velocities make the inertia terms in the momentum equations negligible with respect to the viscous and the pressure forces. In the region of small velocities the magnitude of the pseudo-transient terms used to converge the equations is negligible. As a consequence the diagonal dominance of the coefficient matrix is reduced locally and the iterative scheme is less stable (Rice et al., 2006). In addition, the slower the rotation rate, the lower the effective shearing of the thixotropic material is and the more dependent the overall flow pattern is on the treatment of the low shear viscosity. Then the effectiveness of rheological models, which relate apparent behaviour rather that the complex instabilities that take place in reality and which are regularized so as to be implemented, is reduced.

5. Discussion and conclusions

The experimental and numerical uncertainties previously cited cannot explain the radical change of the measured flow pattern between $N = 2\ s^{-1}$ and $N = 1\ s^{-1}$. At $N = 1\ s^{-1}$, the radial velocity components prevail throughout the cavern, indicating a poor mixing efficiency. For both the models tested and at all stirring rates used here the simulations are unable to capture this behaviour. As stated by Coussot et al. (1993), the rheology of dispersed systems in a low weight molecular matrix is sensitive to sample preparation and to some undesirable effects, such as wall slip, fracture, crack propagation and evaporation. When $N = 1\ s^{-1}$ and $2\ s^{-1}$, the fluid inside the cavern is almost isolated from its surroundings. Moreover, PIV measurements require exposure times of only several minutes. As a consequence, fracture, crack propagation and evaporation are believed to have a weak influence on the measured flow patterns.

To avoid possible wall slip effect, waterproof sand paper with a roughness of about 76 μm (Struers, Champigny sur Marne, France) was glued on the impeller surfaces. Fig. 6 shows both the initial impeller (Fig. 6a) and the impeller covered with sand paper (Fig. 6b). Then the experiment at $N = 1\ s^{-1}$ was repeated using the modified impeller. Fig. 7 shows the

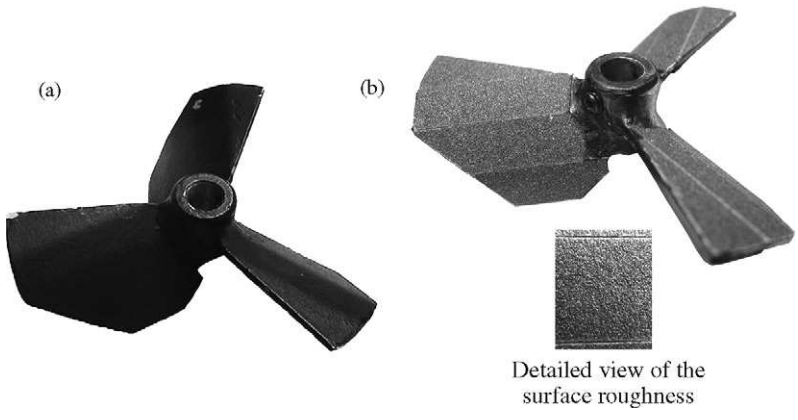

Fig. 6 – Photographs of the Mixel TT impeller used in this study. (a) The original smooth surfaces. (b) Covered with sand paper to avoid wall slip (76 μm).

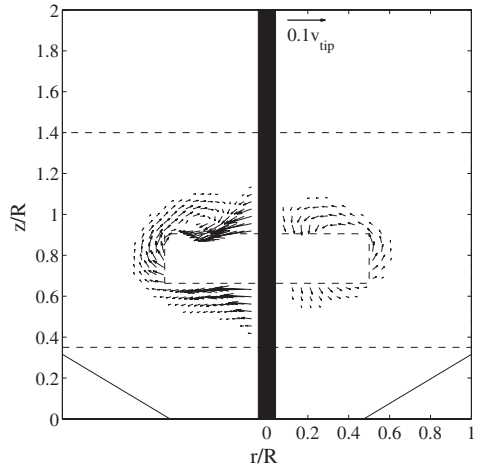

Fig. 7 – The mean planar measured velocity fields at $N = 1\,s^{-1}$ obtained using the smooth-walled impeller (left) and with the rough-walled impeller (right).

mean planar velocity fields measured using PIV at $N = 1\,s^{-1}$ with the smooth-wall impeller (left-hand side) and with the rough-wall impeller (right-hand side). The influence of surface roughness on the flow patterns is obvious, since radial velocity components no longer prevail. The centre of the secondary circulation loop may have shifted into the volume swept by the impeller. Hence, the design modification of the impeller results in improved circulation inside the cavern, since it modifies the Q_a/Q_r ratio ($Q_a/Q_r = 2.1$) but has no or little influence on either the pumping ($Fl = 0.02$) or on the cavern volume ($V_c/V = 3.0$). In Fig. 8, radial profiles of the normalized axial velocity (Fig. 8a) and radial profiles of the normalized radial velocity (Fig. 8b) at the lowest plane swept by the impeller are shown. Contrary to the velocity component which is normal to the lowest plane of the volume swept by the impeller, its tangential component in the radial-axial plane (that is the radial component at the lowest plane of the impeller swept volume and the axial component at the lateral plane of the impeller swept volume) is greatly affected by the surface roughness of the impeller. The Q_a/Q_r ratio is consequently more design-dependant than the flow number. According to Fig. 8b, modifying the surface roughness of the impeller mostly resolves the discrepancies between the measured and simulated velocity data.

In this paper, novel experimental and computational results for the steady-state three-dimensional flow of a thixotropic fluid exhibiting yield stress in a stirred tank were presented. Three stirring rates were examined, namely 1, 2 and $8\,s^{-1}$. The fluid viscosity was determined experimentally and was modelled using two shear-dependant laws, one of which takes account of the basic flow instabilities at small shear rates. They were regularized and implemented in a commercial CFD code using user-defined functions. Experimental study, modelling and simulation of the steady-state flow of such a fluid was delicate because of its complex intrinsic characteristics, including flow instabilities, aging and wall slip effects. Experiments revealed the familiar bulk-flow behaviour characterized by a flow pattern similar to that reported in the literature in the turbulent regime at a rotation rate of $8\,s^{-1}$ and by the formation of caverns around the impeller at smaller rotation rates. It was found that as this rotation rate was reduced, the pumping capacity of the impeller was reduced as well (until becoming almost zero) and that the flow was greatly reorganized leading to poor mixing efficiency. Numerical simulations captured the essential features of the flow, such as cavern formation, the location of recirculation regions and the overall magnitude of the velocities. The predictions from both models were similar in the sheared regions. Experimental and numerical difficulties associated with small convective velocities, together with the necessity of regularising the models, explained the larger discrepancies observed elsewhere. If the exact localization of the sheared/unsheared interface is not of primary interest, use of typical yield-stress fluid models, such as the Herschel–Bulkley law, in simulations is suitable. In addition, the unusual flow pattern determined experimentally at a rotation rate of $1\,s^{-1}$ was found to be due to wall slip effects. Indeed, modifying the impeller design, by gluing sand paper on its surface, resulted in a more 'typical' flow pattern being observed. However, extensive experimental work remains to be done so as to quantify the influence of impeller surface roughness on the overall performance of the system in a wide range of experimental configurations.

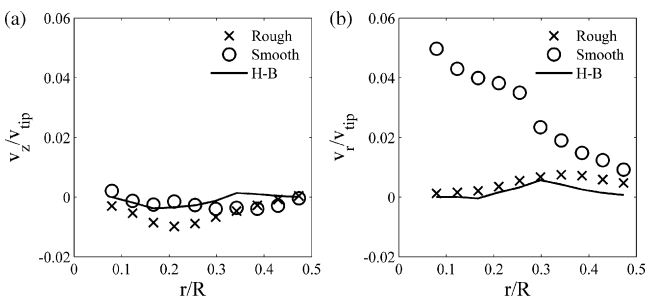

Fig. 8 – Comparison between the experimental ((×) rough surfaces, (o) smooth surfaces) and the numerical ((+) H–B model) radial profiles of the normalized velocity taken at the lowest plane of the impeller swept volume ($z/R = 0.64$) at $N = 1\,s^{-1}$. (a) Axial component v_z. (b) Radial component v_r.

Acknowledgement

The first author (G. Couerbe) acknowledges the financial support of the French government.

REFERENCES

Alexandrou, A.N., Le Menn, P., Georgiou, G. and Entov, V., 2003, Flow instabilities of Herschel–Bulkley fluids. J Non-Newtonian Mech, 116(1): 19–32.

Amanullah, A., Hjorth, S.A. and Nienow, A.W., 1998, A new mathematical model to predict cavern diameters in highly shear thinning, power law liquids using axial flow impellers. Chem Eng Sci, 53(3): 455–469.

Arratia, P.E., Kukura, J., Lacombe, J. and Muzzio, F.J., 2006, Mixing of shear-thinning fluids with yield stress in stirred tanks. AIChE J, 52(7): 2310–2322.

Aubin, J., Mavros, P., Fletcher, D.F., Bertrand, J. and Xuereb, C., 2001, Effect of axial agitator configuration (up-pumping, down-pumping, reverse rotation) on flow patterns generated in stirred vessels. Trans. IChemE, Part A, Chem Eng Res Des, 79(A8): 845–856.

Aubin, J., Le Sauze, N., Bertrand, J., Fletcher, D.F. and Xuereb, C., 2004, PIV measurements of flow in an aerated tank stirred by a down- and an up-pumping axial flow impeller. Exp Therm Fluid Sci, 28(5): 447–456.

Bercovier, M. and Engelman, M., 1980, A finite-element method for incompressible non-Newtonian flows. J Comput Phys, 36(3): 313–326.
Beris, A.N., Isamopoulos, J.A., Armstrong, R.C. and Brown, R.A., 1985, Creeping motion of a sphere through a Bingham plastic. J Fluid Mech, 158: 219–244.
Bonn, D., Tanase, S., Abou, B., Tanaka, H. and Meunier, J., 2002, Laponite: aging and shear rejuvenation of a colloidal glass. Phys Rev Lett, 89(1): 015701.
Cheng, D.C.-H., 2003, Characterization of thixotropy revisited. Rheol Acta, 42(4): 372–382.
Coussot, P., Leonov, A.I. and Piau, J.-M., 1993, Rheology of concentrated dispersed systems in a low molecular weight matrix. J Non-Newtonian Fluid Mech, 46(2–3): 179–217.
Coussot, P., Nguyen, Q.D., Huynh, H.T. and Bonn, D., 2002, Avalanche behaviour in yield stress fluids. Phys Rev Lett, 88(17): 175501.
Escudier, M.P. and Presti, F., 1996, Pipe flow of a thixotropic liquid. J Non-Newtonian Fluid Mech, 62(2–3): 291–306.
Ferroir, T., Huynh, H.T., Chateau, X. and Coussot, P., 2004, Motion of a solid object through a pasty (thixotropic) fluid. Phys Fluids, 16(3): 594–601.
Lamberto, D.J., Alvarez, M.M. and Muzzio, F.J., 1999, Experimental and computational investigation of the laminar flow structure in a stirred tank. Chem Eng Sci, 54(7): 919– 942.
McDonald, R.R. and Anderson, R.S., 1996, Constraints on eolian grain flow dynamics through laboratory experiments on sand slopes. J Sediment Res, 66(3): 642–653.
Nouri, J.M. and Whitelaw, J.H., 1990, Flow characteristics of stirred reactors with Newtonian and non-Newtonian fluids. AIChE J, 36(4): 627–629.
O'Donovan, E.J. and Tanner, R.I., 1984, Numerical study of the Bingham squeeze film problem. J Non-Newtonian Fluid Mech, 15(1): 75–83.
Papanastasiou, T.C., 1987, Flows of materials with yield. J Rheol, 31(5): 385–404.
Papanastasiou, T.C. and Boudouvis, A.G., 1997, Flows of viscoplastic materials: models and computations. Comp Struct, 64(1): 677–694.
Pignon, F., Magnin, A. and Piau, J.-M., 1996, Thixotropic colloidal suspensions and flow curves with minimum: identification of flow regimes and rheometric consequences. J Rheol, 40(4): 573–587.
Poole, R.J. and Escudier, M.P., 2003, Turbulent flow of non-Newtonian liquids over a backward-facing step. Part I. A thixotropic and shear-thinning liquid. J Non-Newtonian Fluid Mech, 109(2–3): 177–191.
Ranade, V.V., 1997, An efficient computational model for simulating flow in stirred vessels: a case of Rushton turbine. Chem Eng Sci, 52(24): 4473–4484.
Rice, M., Hall, J., Papadakis, G. and Yianneskis, M., 2006, Investigation of laminar flow in a stirred vessel at low Reynolds numbers. Chem Eng Sci, 61(9): 2762–2770.
Thompson, D.W. and Butterworth, J.T., 1992, The nature of laponite and its aqueous dispersions. J Colloid Interface Sci, 151(1): 236–243.
Willenbacher, N., 1996, Unusual thixotropic properties of aqueous dispersion of Laponite RD. J Colloid Interface Sci, 182(2): 501–510.
Zhu, H., Kim, Y.D. and De Kee, D., 2005, Non-Newtonian fluids with a yield stress. J Non-Newtonian Fluid Mech, 129(3): 177–181.